Unveiling and utilizing the reconstructing dynamics on nanoporous Ag-Bi for CO_2 electroreduction

Xiangji Zhou [a], Yongqi Liu [a], Lin Liu [b], Yao Yu [b], Jiangang Xu [c], Min Ruan [d,*], Song Li [e,*], Lihua Qian [a,*]

[a] School of Physics, Huazhong University of Science and Technology, Wuhan 430074, China
[b] School of Materials Science and Engineering, State Key Lab for Materials Processing and Die & Mold Technology, Wuhan National High Magnetic Field Center, Huazhong University of Science and Technology, Wuhan 430074, China
[c] Chongyang County Public Inspection and Testing Center, Chongyang 437599, China
[d] Hubei Key Laboratory of Mine Environmental Pollution Control & Remediation, Hubei Polytechnic University, Huangshi 435003, China
[e] School of Materials Science & Engineering, Key Lab Anisotropy & Texture Mat MoE, Northeastern University, Shenyang 110167, China

ARTICLE INFO

ABSTRACT

The reconstruction of catalysts during electrochemical reactions has become an unavoidable issue for higher catalytic activity and the intrinsic mechanism. Herein the reconstruction that amorphous Bi shell forming onto nanoporous AgBi during CO_2ER is regulated by potential, and the optimal reconstruction potential is confirmed to be − 1.05 V. The surface reconfiguration and catalytic property conversion along with the reconstruction are identified via in-situ electrochemical and spectroscopic characterizations. The reconstructed catalyst achieves a Faradaic efficiency of 94 %, partial current density of 19.75 mA•cm^{-2}, and wonderful durability, thanks to the special nanoporous core-shell structure with abundant defects and a efficient electron transport. Furthermore, computational simulation manifests that Bi atoms on the ligament surface are more capable to activating CO_2 than Ag atoms. This investigation introduces one method to elucidate the real state of catalysts and proposes a novel strategy for designing electrochemical catalysts with high activity and durability by atomic scale reconstruction.

1. Introduction

CO_2 electroreduction (CO_2ER) enables the conversion of CO_2 molecules to highly value-added fuels in ambient environments, which is a crucial step for carbon neutralization, and sustainable development of global environment. Many efforts have been made to synthesize electrochemical catalysts with high activity and selectivity in the last decade [1–3]. Hitherto, some catalysts exhibit outstanding conversion efficiency for various productions [4–7]. However, there's a growing awareness that the catalysts usually endure inevitable reconstruction throughout electrochemical reactions at high overpotential, in accompany with uncertain strengthening and deterioration of ultimate catalysis [8,9]. In recent years, irreversible reconstructions at multiple scales were reported on various catalysts including nanoparticles [10, 11], nanosheets [4,12], and porous alloys [13,14], which were experimentally identified by microscopic observations and spectroscopic techniques [15,16].

In our investigations, nanoporous Au holds superb selectivity and Faradaic efficiency (FE) for CO production due to superior activity at atomic steps [17]. However, the irreversible reconstructions from these steps to crystalline facets with unsatisfied selectivity are experimentally monitored by underpotential deposition of Pb [18]. Alloy catalysts

---

usually also suffer surface reconstruction from equilibrium alloys to metastable and even amorphous phases in an irreversible manner. Randomly dispersed Cu clusters aggregated onto nanoporous $Ag_{99.1}Cu_{0.9}$ exhibit higher FE for CO production than nanoporous Ag without Cu skin, and local electronic structure benefits to electrochemical activation of CO_2 molecules with the appearance of strengthening selectivity [19]. Besides CO_2 to CO conversion, formate is normally obtained from bismuth (Bi) and Bi-derivative materials [20–23]. Surface reconstructions of these catalysts are also experimentally demonstrated in recent years. In-situ Raman spectroscopy in combination with ex-situ electron microscopy reveals the intricate reconstructing dynamics of Bi-based metal-organic framework toward Bi nanosheets or their corresponding oxides [24–26]. Those reconstructed Bi catalysts hold great activity and selectivity for formate production, while the reconstruction condition in favor of better catalysis is rarely explored. Our previous work interprets the thermal and dynamic mechanism of an amorphous Bi shell forming on nanoporous AgBi during CO_2ER [27], thereby enabling the strategy to optimize the catalysis by adjusting the reconstruction condition. Besides, although excellent FE and current density were reported in previous investigations [28,29], there are still debates on the real composition and valence state of the catalysts during CO_2ER. There is an urgent desire to unveil the authentic component of the reconstructed surface with high activity and its intrinsic correlation with key intermediate species.

Herein, the potential for the optimal reconstruction of nanoporous AgBi (np-AgBi) for the best catalytic property is explored and ascertained to be − 1.05 V verses reversible hydrogen electrode. Both the reconstructed shell and intermediate species are simultaneously detected in real time when the CO_2ER occurs onto np-AgBi, interpreting the modulation effect of the reconstruction to the catalytic property. The catalyst that endured the optimal reconstruction performs remarkable catalysis for formate production and excellent durability. Spectra characterizations and computational calculations demonstrate that the outstanding catalytic performance is derived from the fast electron transport from Ag to Bi, high active defects, and efficient CO_2 activation on the amorphous Bi shell.

2. Experimental procedures

2.1. Preparation of nanoporous Ag-Bi (np-AgBi)

Precursor $Ag_{20}Al_{79.5}Bi_{0.5}$ (atom ratio) are fabricated as alloy ribbons by having Ag (99.99 %), Al (99.99 %) and Bi (99.99 %) arc-melting and subsequently melt-spinning in an Ar atmosphere. The alloy ribbons are tailored and polished to be 5 mm × 5 mm × 80 μm foils, and got dealloyed in 5 wt% HCl solution for 10 hrs at 60 °C to selectively remove the Al, then rinsed repeatedly with deionized water and dried in Ar atmosphere to obtain np-AgBi consequently. The geometric area of the np-AgBi electrodes in our work is 0.2–0.25 cm^{-2}.

2.2. Surface reconstruction of np-AgBi and preparation of rnp-AgBi-1.05

In previous work, as np-AgBi is used for CO_2 electroreduction, Bi atomic volume diffusion from the interior to the surface of np-AgBi would be triggered by reaction potential, forming a conformal ultrathin amorphous BiO_x shell as a result. Thus, the np-AgBi reconstructed at the potential of − 1.05 V is named rnp-AgBi-1.05 [27].

2.3. Microstructure characterizations

X-ray diffraction (XRD) is obtained by θ-2θ scans using an Empyrean with Cu-Kα radiation. The micromorphology and chemical compositions are characterized by a scanning electron microscope (Nova NanoSEM 450). The exact element contents of np-AgBi samples are measured by inductively coupled plasma-optical emission spectrometry (ICP-OES, Prodigy Plus). High-resolution transmission electron microscopy

(HRTEM) and element mapping are used to observe the morphology and elemental distribution of np-AgBi and rnp-AgBi-1.05. The chemical states of the catalysts are investigated by X-ray photoelectron spectroscopy (XPS, AXIS-ULTRA DLD-600 W), where the binding energy is corrected by reference to the C 1 s signal at 284.5 eV.

2.4. In situ Raman spectroscopy

Raman spectra are carried out at a confocal microscope (Ramos S120, Ostec-ArtTool, LLC, Moscow) with a He/Ne laser of λ = 532 nm (15 mW). To synthesize the working electrode, 5 mg np-AgBi is ultrasonic in the mixture of 50 μL Nafion (5 wt%) and 950 μL for 1 h. Meanwhile, the rectangular slices of carbon fiber paper (5 ×5 mm) are ultrasonic cleaned in ethanol and then rinsed with deionized water. Subsequently, the working electrodes are prepared by dropping the catalyst ink on the clean carbon paper with a loading level of 1 mg cm^{-2}. A carbon rod electrode and a Ag/AgCl electrode are used as the counter electrode and reference electrode, respectively. A specially customized electrolytic cell is used for the in situ Raman spectroscopy. Raman spectra are collected during CO_2ER at a certain potential.

2.5. Electrochemical measurements

All CO_2ER and electrochemical characterizations are conducted on a CHI 760E electrochemical working station (CH instrument, Shanghai, China). A three-electrode H type cell is used as the electrolytic cell, where the np-AgBi foil, Pt electrode and a Ag/AgCl electrode are used as the working electrode, counter electrode and reference electrode, respectively. If not mentioned specifically, all potentials in this letter are versus reversible hydrogen electrode (RHE). Prior to CO_2ER, multiple CV is supplied onto the np-AgBi (the potential range is 0.3–0.76 V, the scan rate is 5 mV s^{-1}) to remove the Bi atoms on the surface. Bi content on the surface of the catalyst is measured based on the oxidation peaks in LSV curves (scan rate of 30 mV s^{-1}). To get the C_{dl} of the catalysts, CV tests are performed at − 0.21 ~ − 0.11 V with different scanning rates (5 ~ 60 mV s^{-1}). C_{dl} is obtained from the linear fitting of the charge-discharge current density at − 0.16 V with the scan rates. EIS is measured in the frequency from 10^6~1 Hz, with a potential of − 0.85 V and an amplitude of 10 mV. Herein, all parameters are normalized by geometry area ($cm^{-2} = cm^{-2}_{geo}$) unless otherwise stated.

2.6. CO_2ER and product analysis

CO_2 gases are pumped into both chambers of the electrolytic cell at a rate of 10 sccm for 30 min before CO_2ER. The gas products are detected by gas chromatography (GC) and liquid products are examined by proton nuclear magnetic resonance spectroscopy (H NMR, Bruker Avance- 500 MHz), with dimethyl sulfoxide (DMSO) and deuterium oxide (D_2O) as the reference and solvent, respectively.

3. Results and discussions

3.1. Characterization of rnp-AgBi-1.05 and observation of the surface reconstruction

Nanoporous Ag-Bi (np-AgBi) is synthesized by chemical dealloying of $Ag_{20}Al_{79.5}Bi_{0.5}$ (at%). Electron microscopies in Fig. S1 reveal the spatially interconnected skeletons of AgBi ligaments with an average diameter of 85 nm. The uniform distribution of Bi atoms on the ligaments is identified by element mapping. As reported in previous work, the reconstruction that Bi atoms diffuse from internal skeletons to skin and create an ultrathin disordered Bi shell subsequently would occur during CO_2ER at room temperature [13]. Fig. 1 shows the morphological structure of the reconstructed catalyst rnp-AgBi-1.05, which is obtained by having the pristine np-AgBi subjected to 135 min CO_2ER at − 1.05 V
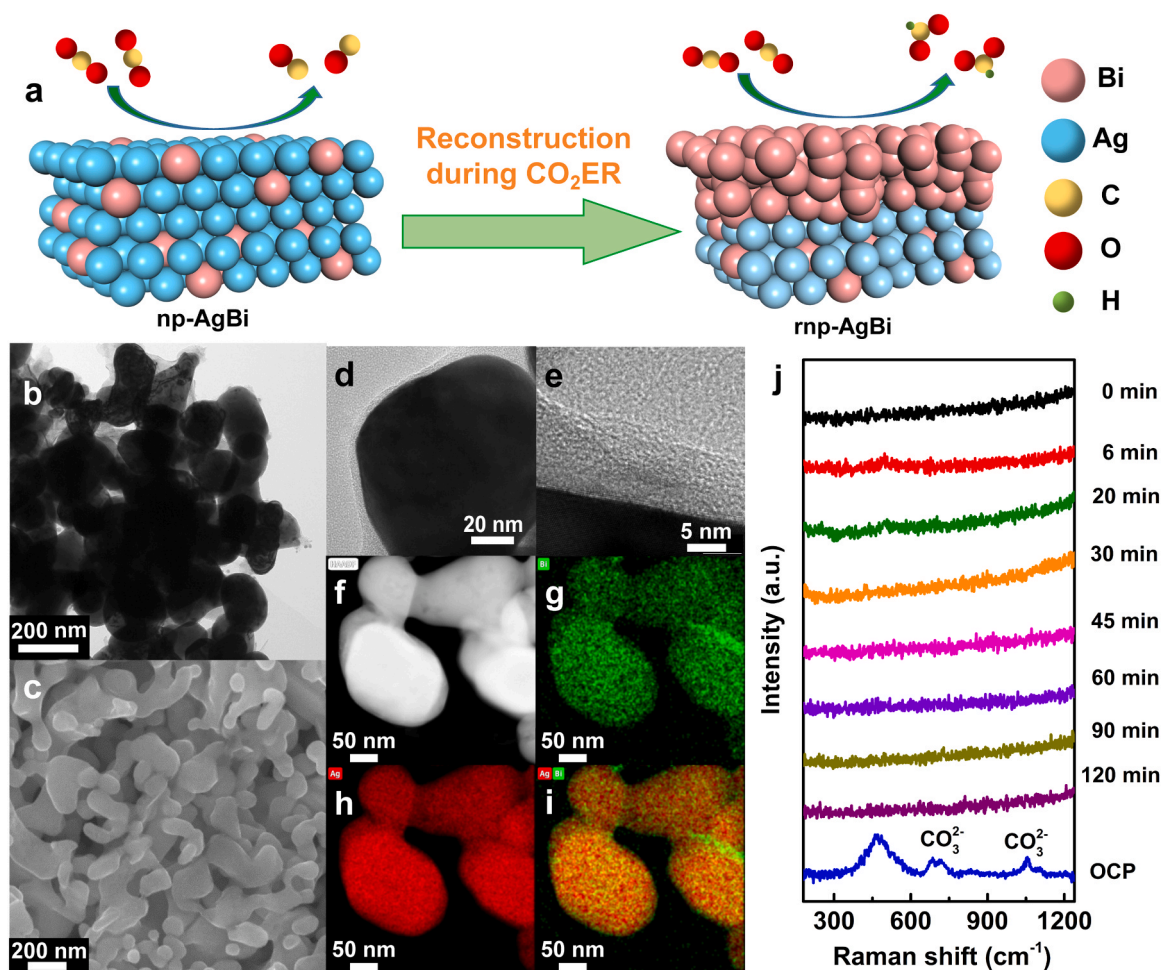
Fig. 1. Surface morphology and microstructure of the reconstructed catalyst rnp-AgBi-1.05. (a) Schematic illustration of surface reconstruction and the catalysis. (b) TEM, (c) SEM, (d-e) HRTEM images, (f) HAADF and (g-i) element mappings of rnp-AgBi-1.05. (j) In-situ Raman signal of np-AgBi measured at different time of CO_2ER under the potential of -1.05 V.

vs. RHE (Fig. 1(a)). Transmission electron microscopy (TEM) and scanning electron microscopy (SEM) in Fig. 1(b-c) identify that the nanoporous infrastructures are retained. Meanwhile an 8.92 nm layer of amorphous BiO_x is observed by high-resolution TEM (HRTEM) in Fig. 1 (d-e). High-angle annular dark field (HAADF) and element mapping in Fig. 1(f-i) confirm the conformal covering of amorphous BiO_x on the internal skeletons. Except for the newborn amorphous shell, a single-phase AgBi solid solution can be inherited in rnp-AgBi-1.05 after 135 min of CO_2ER based on X-ray diffraction patterns (XRD) in Fig. S2. X-ray photoelectron spectroscopy (XPS) in Fig. S3 indicates that the proportion of Bi^0 in rnp-AgBi-1.05 is much less than that in np-AgBi, which is consistent with the appearance of amorphous BiO_x shell. It is necessary to identify the real state of the Bi during the CO_2ER. The broad peaks at 470 cm^{-1} (P_{Bi-O}) in Fig. 1(j) are assigned to the Bi-O photo-luminescence of amorphous BiO_x [30]. It is worth noting that the P_{Bi-O} band in Raman spectroscopy is absent when CO_2ER is taking place on np-AgBi, whereas the P_{Bi-O} band appears immediately when the CO_2ER temporarily halts (in a state of open circuit potential, OCP). Therefore, Bi atoms on the ligaments are in the metallic state (Bi^0) during the CO_2ER, and get oxidized soon after terminating the reaction. Dynamic conversion of Bi valence state at the catalyst/electrolyte interface indicates the vigorous activity of the metallic amorphous Bi shell for CO_2ER.

3.2. Catalysis optimization via surface reconstruction

Nowadays, the reconstruction of catalyst could be considered as a strategy to design highly active catalysts [31–34]. As interpreted in our previous work, the reconstructing saturation could be modulated by the electrochemical potential of CO_2ER, enabling the tunable thickness of Bi shells [27]. To study the effect of shell thickness on catalytic activity, rnp-AgBi-*n* catalysts are synthesized from np-AgBi reconstructed at six different potentials (here *n* represents different potentials from -0.85 to -1.10 V). Fig. 2(a) exhibits the in-situ Raman spectra of the np-AgBi that experiences CO_2ER at various potentials, inducing the subsequent creation of rnp-AgBi-*n*. The P_{Bi-O} vanishes immediately when the potentials are supplied and shows up as the potential turns to OCP, which is in agreement with Fig. 1(j). Since the Raman signal of metallic Bi is invisible, the intensity of P_{Bi-O} is used to represent the aggregation of Bi on the surface of np-AgBi. Notably, P_{Bi-O} rises monotonously with the reaction potential, verifying that the amorphous Bi shell grows thicker due to the surface reconstruction at higher potential. The HRTEM images in Fig. 2(b-e) show that the amorphous shell thickness of of rnp-AgBi-0.85, rnp-AgBi-0.95, and rnp-AgBi-1.05 are 2.02, 3.97, and 9.04 nm, respectively. Whereas the Bi shell of rnp-AgBi-1.10 is not uniform and contains crystal Bi particles. The difference in rnp-AgBi-1.10 is likely because the reconstruction gets disrupted by the too intensive CO_2ER and HER.

The catalytic performance of rnp-AgBi-*n* are examined. Linear sweep voltammetry in Fig. 2(f) demonstrates that rnp-AgBi-1.05 has the
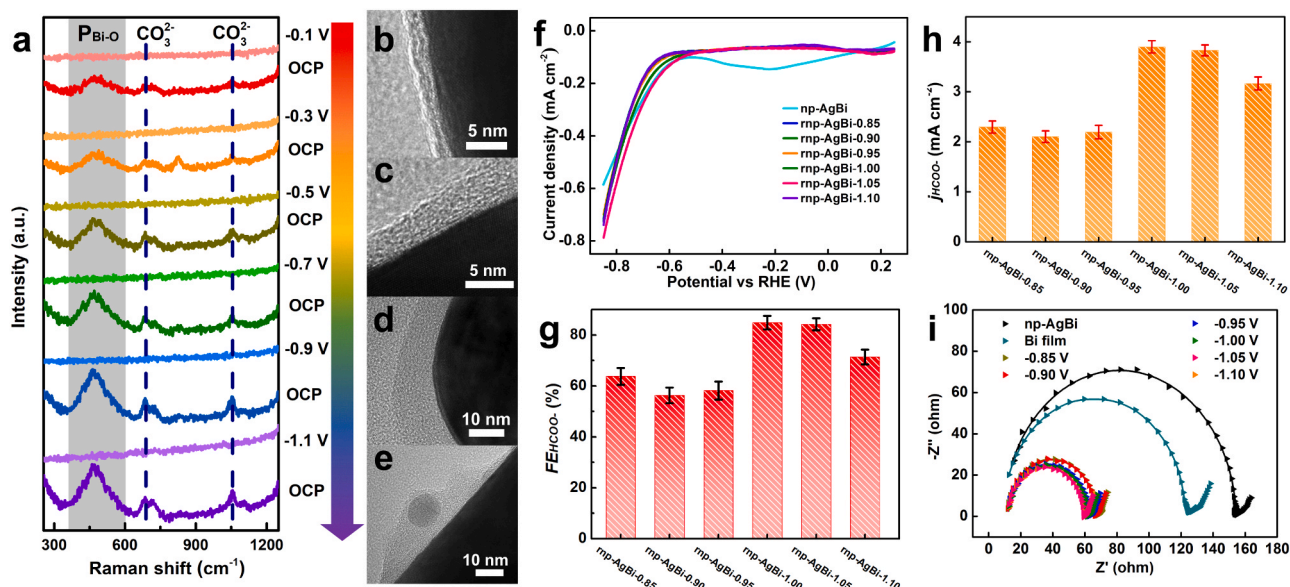
Fig. 2. Structure and CO₂ER performance optimization via the potential modulated reconstruction. (a) In-situ Raman patterns of rnp-AgBi-n that experiences reconstruction at the potential from $-0.1 \sim -1.1$ V. The potential will turn to OCP for 5 min every time after 30 min of reconstruction at different potentials. (b-e) HRTEM images of rnp-AgBi-0.85, rnp-AgBi-0.95, rnp-AgBi-1.05 and rnp-AgBi-1.10 respectively. (f) LSV curves of rnp-AgBi-n. (g) FE_{HCOO^-} and (h) j_{HCOO^-} of all the rnp-AgBi-n tested at -0.85 V. (i) EIS of np-AgBi, Bi film and all the rnp-AgBi-n.

highest current densities in CO₂ saturated 0.1 M KHCO₃. The rnp-AgBi-n catalysts are performed at -0.85 V, in which condition surface reconstruction no longer occurs. The rnp-AgBi-1.00 and rnp-AgBi-1.05 in Fig. 2(g-h) hold the highest faradaic efficiency (FE_{HCOO^-}, about 84.8 %) and partial current density (j_{HCOO^-}, about 3.9 mA cm⁻²) for HCOO⁻ production, where the liquid product is quantitatively monitored through ¹H nuclear magnetic resonance (¹HNMR) in Fig. S4. The outstanding activity of rnp-AgBi-1.05 is probably attributed to its thickest, uniform, and amorphous Bi shell, as the defects distributed in the disordered Bi shell play the critical roles for CO₂ absorption and activation [35]. To confirm our hypothesis, electrochemical impedance spectroscopies (EIS) of np-AgBi, crystal Bi film and all the rnp-AgBi-n are depicted in Fig. 2(i), from which charge-transfer resistance R_{ct} is

estimated (showed in Fig. S5). On one hand, the R_{ct} of all rnp-AgBi-n are much smaller than that of the np-AgBi (139.3 Ω) and Bi film (114 Ω), confirming that amorphous Bi shell with good conductivity benefits the charge transfer between the catalysts and the intermediates [36]. On the other hand, the rnp-AgBi-1.05 (47.3 Ω) holds the smallest R_{ct}, indicating that the catalyst possesses the highest catalysis could be obtained when np-AgBi is reconstructed at -1.05 V. In general, different levels of surface reconstruction can be feasibly tailored by electrochemical potential, thus the catalytic activity of the outer shell can be tuned in favor of the electrocatalysis, while the rnp-AgBi-n with the best catalysis is created at the optimal potential of -1.05 V due to its thickest uniform amorphous shell and most active defects.
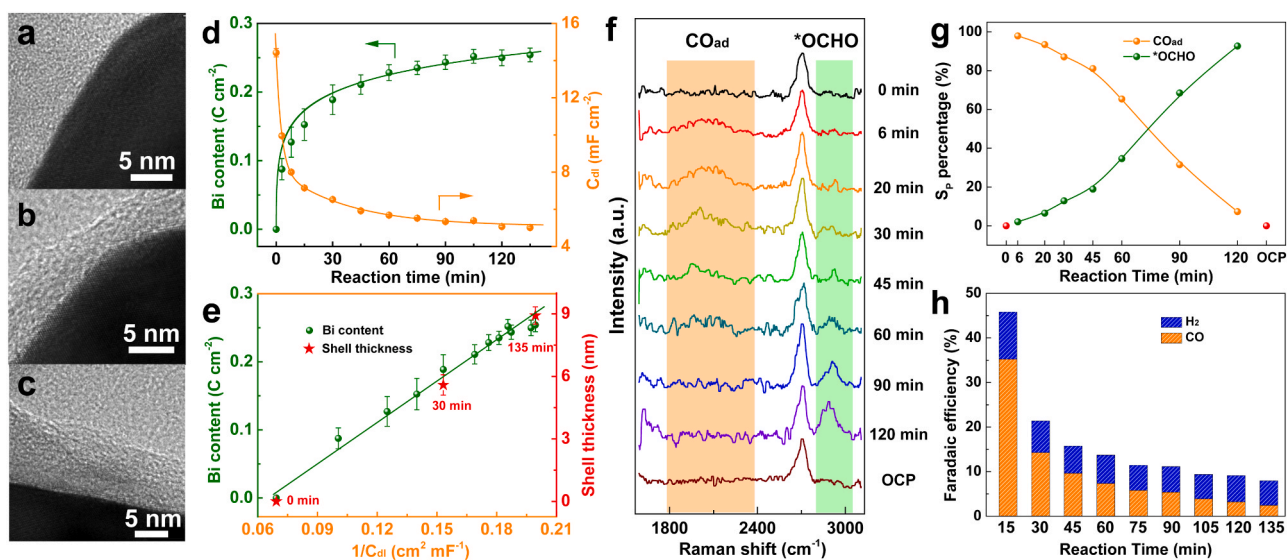
Fig. 3. Evolution of the catalyst structure and product selectivity as np-AgBi reconstructing to np-AgBi-1.05. (a-c) HRTEM of np-AgBi that experiences 0, 30, and 135 min CO₂ER at -1.05 V, respectively. (d) Time dependence of calculated C_{dl} and Bi content. (e) Linear relation between $1/C_{dl}$, Bi content, and shell thickness. (f) In-situ Raman spectra of np-AgBi at different time of CO₂ER. (g) Relative intensity of Raman peaks (S_p) corresponding to CO$_{ad}$ and *OCHO respectively. (h) Faradaic efficiency of gases products tested at different time of CO₂ER.

### 3.3. Evolution of catalytic properties of np-AgBi with surface reconstruction

To understand the mechanism of the catalysis optimization during CO_2ER, in situ characterizations on the evolution of the structure and intermediates are necessary. Fig. 3(a-c), Fig. S6 show that the shell thicknesses of amorphous BiO_x are 0, 5.95, and 9.04 nm for the rnp-AgBi-1.05 after 0, 30, and 135 min CO_2ER, respectively. Our previous work introduced the way to monitor the formation of the amorphous Bi shell via in-situ characterizations of electrochemical oxidization and electrochemical double layer capacitance (C_{dl}) [27]. The growing of Bi shell at the potential of − 1.05 V is presented in Fig. 3(d), Fig. S7 and Fig. S8, where the time dependence of surface Bi content and C_{dl} indicate that the reconstruction is rapid in the beginning and gets to a limit ultimately. Significantly, linear relationships between the shell thickness, Bi content and the reciprocal C_{dl} is demonstrated in Fig. 3(e) [37]. Therefore, Bi content and $1/C_{dl}$ are reliable rulers to determine shell thickness. In addition, although the C_{dl} decreases monotonously as the reconstruction goes on, the electrochemical surface area (ECSA) of np-AgBi increases. Fig. S9 illustrates that the C_{dl} per unit area of Ag (79.77 $\mu F\ cm^{-2}$) is four times larger than that of Bi (20.72 $\mu F\ cm^{-2}$) in the case of identical geometry and morphology. Based on the calculation in the supplementary materials, ECSA of rnp-AgBi-1.05 (242 $cm^2_{ECSA}\ cm^{-2}$) is 1.3 times higher than that of pristine np-AgBi (181 $cm^2_{ECSA}\ cm^{-2}$), indicating the catalysis enhancement for CO_2ER [38,39].

The intermediate species absorbed on np-AgBi during CO_2ER are investigated by in-situ Raman spectroscopy (Fig. 3(f)). The Raman band at 2700 cm^{-1}, corresponding to the G′ mode of graphite, is used as an internal calibration [40]. The band at 2050 cm^{-1} is CO adsorbate (CO_{ad}), and the band at 2900 cm^{-1} is the C-H stretching of *OCHO adsorbate [41–43]. Raman bands of CO_{ad} and *OCHO are nearly blank prior to CO_2ER. Raman band CO_{ad} becomes relatively visible in the early stage of CO_2ER (from 6 to 45 min), which correlates with Ag atoms on the ligament with considerable selectivity toward CO production. However, this Raman band gradually becomes weak and disappears with further reaction. By comparison, the Raman band of *OCHO adsorbate is not obvious until 45 min, indicating the production of $HCOO^-$. Subsequently, its intensity shows everlasting increment and saturates at 120 min. These two bands disappear immediately when the electrochemical potential shuts down. To visualize the temporal evolution of these dual intermediates, relative intensity of the Raman peaks (S_p) corresponding to CO_{ad} and *OCHO are calculated and depicted in Fig. 3(g). The opposite variation of these two intermediates with

reaction time demonstrates that CO_2 is predominantly converted toward CO at the initial stage and then toward formate. As the potential driven reconstruction will result in the uniform covering of Bi atoms onto the ligament surface, the adsorption of $*CO_2$ onto Ag atoms will get obstructed consequently. To quantitatively verify this tendency, FEs of CO and H_2 are detected every 15 min during CO_2ER at − 1.05 V. The overall FE of gas products in Fig. 3(h) decreases sharply from 45.8 % to 10 % with reaction time, implying the FE augmentation of liquid products. Significant suppression of gas products results from the dominant interaction of the reconstructed Bi shell with the intermediates $*CO_2$ and *OCHO.

3.4. Optimized catalytic performance of the rnp-AgBi-1.05

As the rnp-AgBi-1.05 is ascertained to be the catalyst derived from the optimal reconstruction. Fig. S10 exhibits the LSV tests of the rnp-AgBi-1.05 in 0.1 M $KHCO_3$ saturated with N_2 and CO_2, respectively. The rnp-AgBi-1.05 represents much higher current density in 0.1 M $KHCO_3$ saturated with CO_2 in comparison with N_2, manifesting its activity. Fig. 4(a) represents the product selectivity of the rnp-AgBi-1.05 at different potentials, where the FE_{HCOO} is over 90 % at a potential of − 0.95~− 1.05 V and approaches 94 % at − 1.05 V. Fig. 4(b) indicates a specific current density (j_{HCOO}) of 19.75 mA cm^{-2} at − 1.05 V. In comparison with the Bi-based catalysts reported previously, the rnp-AgBi-1.05 developed here shows remarkable activity for CO_2 to $HCOO^-$ conversion (Fig. S11), presenting an $HCOO^-$ productivity of 1.88 mmol $mg^{-1}\ h^{-1}$ at − 1.05 V. Besides the excellent activity, stability test of rnp-AgBi-1.05 is carried out at the potential of − 0.95 V. Fig. 4(c) shows that after 24 hrs CO_2ER, the FE_{HCOO} only has a slight decay from 90.3 % to 87.8 %, while the j_{HCOO} has the increment from 7.8 to 10.2 mA cm^{-2}. The conformal shell with a thickness of 8.99 nm in Fig. 4(d) verifies that the surface morphology of rnp-AgBi-1.05 still retains. Since the newborn Bi shell and the catalytic activity stem from surface reconstruction, it can be expected that the performance will not degrade but may improve [44]. Obviously, the lattice between the amorphous Bi shell and the AgBi core would mismatch in the beginning of CO_2ER, while Fig. 4(e) shows that the interface of the Bi shell and the AgBi core becomes short-range ordered after the stability test, illustrating the better interconnection between the core and shell. Moreover, XPS of the rnp-AgBi-1.05 before and after the stability test are exhibited in Fig. 4 (f-g). The binding energy of Bi^0 shows a positive shift of 0.5 eV while there is no shift on the signals of Bi^{3+} or Ag, which implies the closer bonding between Ag and Bi [45]. Therefore, the increment of j_{HCOO}
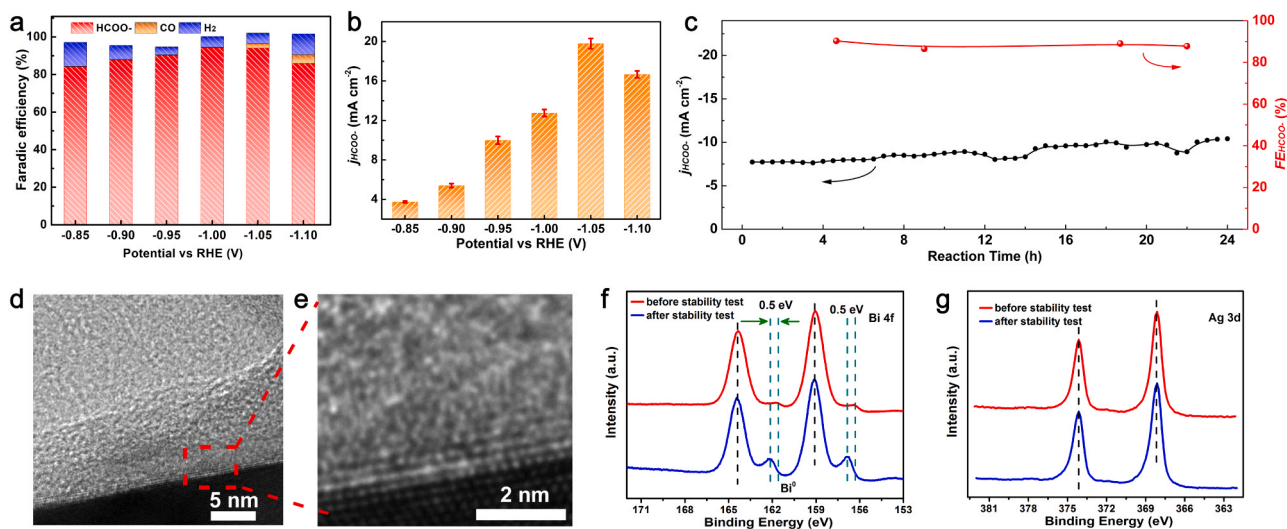
Fig. 4. CO_2ER performance of rnp-AgBi-1.05. (a) FEs of all products and (b) j_{HCOO^-} under different potentials of CO_2ER. (c) CO_2ER catalysis stability test at − 0.95 V for 24 h. (d-e) HRTEM pictures of rnp-AgBi-1.05 after the stability test. (f-g) XPS patterns of the rnp-AgBi-1.05 before and after the stability test.

might be attributed to faster electron transport from the AgBi core to the Bi shell. Whereas the slight decrease of FE_{HCOO^-} is probably due to the deposition of impurity ions from the electrolyte [18,46].

As described above, the outstanding performance of rnp-AgBi-1.05 is attributed to the heterogeneous structure that consists of a nanoporous skeleton, an internal highly conductive alloy core, and an active amorphous Bi shell [14,36,47]. To have further insight into the intrinsic mechanism, density functional theory (DFT) is utilized to estimate the free energy of CO_2ER pathway in Fig. 5(a-b). The calculating models of CO_2ER processes are exhibited in Fig. 5c and Fig. S12, where the Ag (111) surface is covered with the reconstructed Bi shell. The intermediate *OCHO is favorable species to output HCOO⁻ while intermediate *COOH is favorable for CO [48,49]. The positive adsorption free energy of *COOH (0.86 eV) on the Bi site indicates the suppression of CO production. By contrast, moderate adsorption of *OCHO (−0.72 eV) facilitates the high production of HCOO⁻. Meanwhile, the energy difference (0.40 eV) between *CO₂ and *OCHO implies that *OCHO formation is the rate determining step of CO_2 to HCOO⁻ conversion. Moreover, the smaller adsorption free energy of *CO₂ intermediate on the Bi shell manifests that CO_2 tends to be absorbed and activated on Bi (−0.32 eV) rather than Ag (−0.48 eV), consistent with the explanation for the in-situ Raman of the intermediates in Fig. 3(f-g). This simulation demonstrates that product selectivity switching from CO to HCOO⁻ not only results from the Bi atoms geometrically occupying the ligament surface, but also from the higher activity of the Bi atoms than the Ag atoms.

4. Conclusion

In summary, we explore the approach to stimulating the catalytic property of np-AgBi through adjusting its surface reconstruction. The optimal potential for the most active reconstructed Bi shell turns out to be − 1.05 V. With in-situ electrochemical characterization and in-situ Raman spectroscopy, Bi shell forming on the catalyst surface and the corresponding product selectivity conversion from CO to HCOO⁻ are

represented intuitively. The rnp-AgBi-1.05 with the optimal reconstructed structure realizes the catalysis with FE_{HCOO} as high as 94 % and j_{HCOO} of 19.75 mA cm⁻². With the better interconnection between the AgBi core and amorphous Bi shell, the catalysis of rnp-AgBi-1.05 shows incredible improvement but not degradation thanks to the reconfiguration of the core-shell interface. Computational simulation demonstrates that the reconstructed Bi shell holds high activity for CO_2 activation, thus achieving the excellent catalysis. The insight of dynamic reconstruction reported here is instructive for designing active catalysts and understanding the reaction mechanism. Meanwhile, surface reconstruction induced by electrochemical potential could be a simple and feasible method to summit the high activity and durability of catalysts simultaneously.

CRediT authorship contribution statement

Xiangji Zhou: Conceptualization, Investigation, Methodology, Validation, Visualization, Formal analysis, Writing – original draft. **Yongqi Liu:** Data curation, Writing – original draft. **Lin Liu:** Validation, Resources. **Yao Yu:** Visualization, Resources. **Jiangang Xu:** Investigation, Data curation. **Min Ruan:** Software, Data curation. Validation. **Song Li:** Investigation, Writing – review & editing. **Lihua Qian:** Project administration, Funding acquisition, Supervision, Resources, Writing – review & editing.
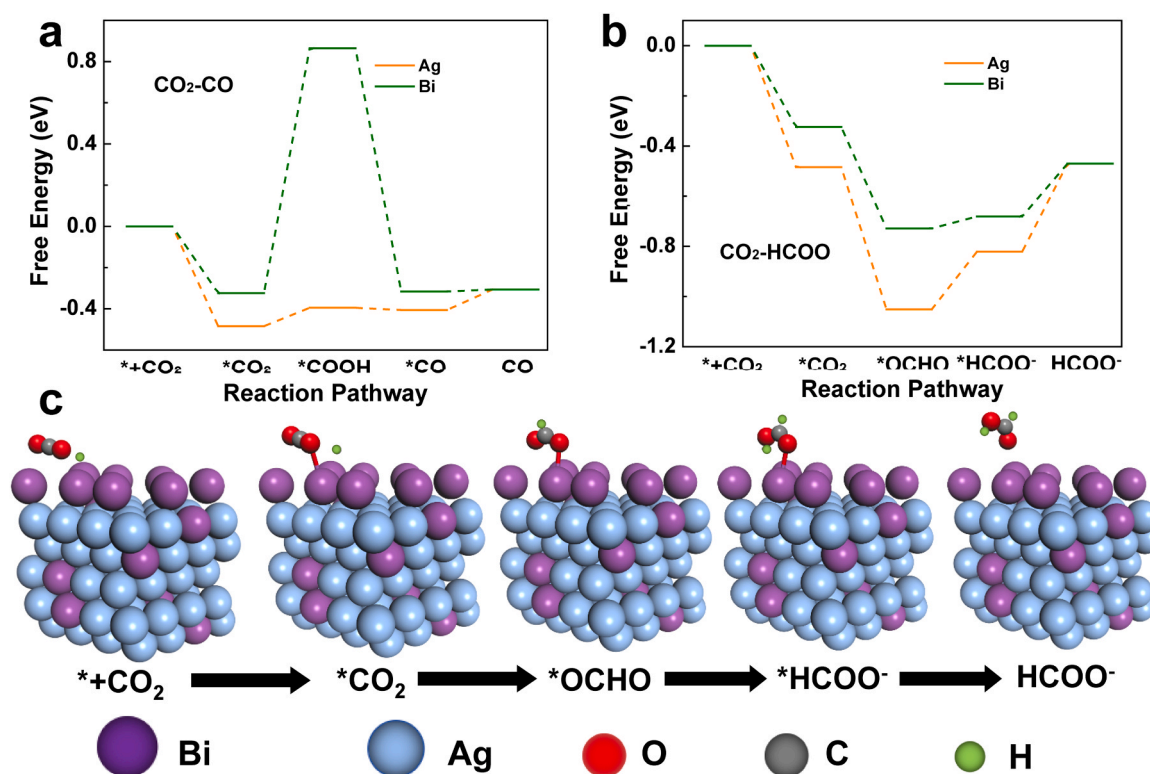
Fig. 5. Computational analysis on the catalytic activity of rnp-AgBi-1.05. (a) DFT calculations of CO_2 to CO process on rnp-AgBi-1.05. (b) DFT calculations of CO_2 to HCOO⁻ process on rnp-AgBi-1.05. (c) Geometric models of intermediates (*+CO₂, *CO₂, *OCHO, *HCOO⁻, HCOO⁻) evolution in the process of CO_2-HCOO⁻ conversion.

Declaration of Competing Interest

The authors declare that they have no conflicts of interest to report.

Data availability

Data will be made available on request.

Acknowledgement

Appendix A. Supporting information

Method for ECSA evaluation. Additional electrochemical and microscopy characterizations of np-AgBi and rnp-AgBi-1.05 (Fig. S1-S3), example of liquid product detection via ^{1}HNMR (Fig. S4), calculation result from the EIS of the catalysts (Fig. S5), characterization of the reconstruction process (Fig. S6-S8), supplementary measurements to interpret the catalytic activity of rnp-AgBi-1.05 (Fig. S9~S11), DFT calculation models for CO_2 to CO conversion (Fig. S12). Supplementary data associated with this article can be found in the online version at doi:10.1016/j.apcatb.2023.123552.

References

[1] A.R. Woldu, Z. Huang, P. Zhao, L. Hu, D. Astruc, Electrochemical CO_2 reduction (CO_2RR) to multi-carbon products over copper-based catalysts, Coord. Chem. Rev. 454 (2022), 214340.

[2] R. Zhao, P. Ding, P. Wei, L. Zhang, Q. Liu, Y. Luo, T. Li, S. Lu, X. Shi, S. Gao, A. M. Asiri, Z. Wang, X. Sun, Recent progress in electrocatalytic methanation of CO_2 at ambient conditions, Adv. Funct. Mater. 31 (2021), 2009449.

[3] F. Yang, A.O. Elnabawy, R. Schimmenti, P. Song, J. Wang, Z. Peng, S. Yao, R. Deng, S. Song, Y. Lin, M. Mavrikakis, W. Xu, Bismuthene for highly efficient carbon dioxide electroreduction reaction, Nat. Commun. 11 (2020) 1088.

[4] Y. Zhang, R. Zhang, F. Chen, F. Zhang, Y. Liu, X. Hao, H. Jin, X. Zhang, Z. Lu, H. Dong, F. Lu, W. Wang, H. Liu, H. Liu, Y. Cheng, Mass-transfer-enhanced hydrophobic bi microsheets for highly efficient electroreduction of CO_2 to pure formate in a wide potential window, Appl. Catal. B Environ. 322 (2023), 122127.

[5] Y. Yu, D. Wang, Y. Hong, T. Zhang, C. Liu, J. Chen, G. Qin, S. Li, Bulk-immiscible CuAg alloy nanorods prepared by phase transition from oxides for electrochemical CO_2 reduction, Chem. Commun. 58 (2022) 11163–11166.

[6] M. Li, Y. Ma, J. Chen, R. Lawrence, W. Luo, M. Sacchi, W. Jiang, J. Yang, Residual chlorine induced cationic active species on a porous copper electrocatalyst for highly stable electrochemical CO_2 reduction to C_{2+}, Angew. Chem. Int. Ed. 60 (2021) 11487–11493.

[7] X. Lv, Q. Liu, J. Wang, X. Wu, X. Li, Y. Yang, J. Yan, A. Wu, H.B. Wu, Grain refining enables mixed Cu^+/Cu^0 states for CO_2 electroreduction to C_{2+} products at high current density, Appl. Catal. B Environ. 324 (2023), 122272.

[8] X. Lin, X. Liu, Y. Zhao, J. Lan, K. Jiang, Z. Liu, F. Xie, Y. Tan, Dynamic surface restructuring of nanoporous Cu_{2-x}Se for efficient CO_2 electroreduction into methanol, J. Energy Chem. 71 (2022) 514–520.

[9] Y. Jiang, X. Wang, D. Duan, C. He, J. Ma, W. Zhang, H. Liu, R. Long, Z. Li, T. Kong, X.J. Loh, L. Song, E. Ye, Y. Xiong, Structural reconstruction of Cu_2O superparticles toward electrocatalytic CO_2 reduction with high C_{2+} products selectivity, Adv. Sci. 9 (2022), e2105292.

[10] Y. Zhu, W. Dai, X. Zhong, T. Lu, Y. Pan, In-situ reconstruction of non-noble multi-metal core-shell oxyfluorides for water oxidation, J. Colloid Interface Sci. 602 (2021) 55–63.

[11] D. Yao, C. Tang, L. Li, B. Xia, A. Vasileff, H. Jin, Y. Zhang, S.Z. Qiao, In situ fragmented bismuth nanoparticles for electrocatalytic nitrogen reduction, Adv. Energy Mater. 10 (2020), 2001289.

[12] Y. Zhao, X. Tan, W. Yang, C. Jia, X. Chen, W. Ren, S.C. Smith, C. Zhao, Surface reconstruction of ultrathin palladium nanosheets during electrocatalytic CO_2 reduction, Angew. Chem. Int. Ed. 59 (2020) 21493–21498.

[13] X. Zhou, X. Lu, T. Yu, H. Wang, L. Qian, P. Lei, Y. Yu, L. Liu, S. Xia, J. Fang, Conformal shell amorphization of nanoporous Ag-Bi for efficient formate generation, ACS Appl. Mater. Interfaces 12 (2020) 31319–31326.

[14] X. Su, Y. Sun, L. Jin, L. Zhang, Y. Yang, P. Kerns, B. Liu, S. Li, J. He, Hierarchically porous Cu/Zn bimetallic catalysts for highly selective CO_2 electroreduction to liquid C_2 products, Appl. Catal. B Environ. 269 (2020), 118800.

[15] X. Liu, R. Guo, W. Huang, J. Zhu, B. Wen, L. Mai, Advances in understanding the electrocatalytic reconstruction chemistry of coordination compounds, Small 17 (2021), e2100629.

[16] H. Xiao, K. Chi, H. Yin, X. Zhou, P. Lei, P. Liu, J. Fang, X. Li, S. Yuan, Z. Zhang, Y. Su, J. Guo, L. Qian, Excess activity tuned by distorted tetrahedron in $CoMoO_4$ for oxygen evolution, Energy Environ. Mater. (2023), e12495.

[17] T. Yu, X. Zhou, Y. Chen, J. Chen, S. Yuan, Z. Zhang, L. Qian, S. Li, Robust catalysis of hierarchically nanoporous gold for CO_2 electrochemical reduction, Electrochim. Acta 437 (2023), 141537.

[18] X. Lu, T. Yu, H. Wang, L. Qian, P. Lei, Electrochemical fabrication and reactivation of nanoporous gold with abundant surface steps for CO_2 reduction, ACS Catal. 10 (2020) 8860–8869.

[19] H. Wang, X. Zhou, T. Yu, X. Lu, L. Qian, P. Liu, P. Lei, Surface restructuring in AgCu single-atom alloy catalyst and self-enhanced selectivity toward CO_2 reduction, Electrochim. Acta 426 (2022), 140774.

[20] J.-W. Shi, S.-N. Sun, J. Liu, Q. Niu, L.-Z. Dong, Q. Huang, J.-J. Liu, R. Wang, Z. Xin, D. Zhang, J. Niu, Y.-Q. Lan, Calixarene-functionalized stable bismuth oxygen clusters for specific CO_2-to-HCOOH electroreduction, ACS Catal. 12 (2022) 14436–14444.

[21] C. Lin, Y. Liu, X. Kong, Z. Geng, J. Zeng, Electrodeposited highly-oriented bismuth microparticles for efficient CO_2 electroreduction into formate, Nano Res. 15 (2022) 10078–10083.

[22] X. Zhang, X. Sun, S.-X. Guo, A.M. Bond, J. Zhang, Formation of Lattice-dislocated Bismuth Nanowires on Copper Foam for Enhanced Electrocatalytic CO_2 reduction at low overpotential, Energy Environ. Sci. 12 (2019) 1334–1340.

[23] Y.X. Duan, Y.T. Zhou, Z. Yu, D.X. Liu, Z. Wen, J.M. Yan, Q. Jiang, Boosting production of HCOOH from CO_2 electroreduction via Bi/CeO_x, Angew. Chem. Int. Ed. 60 (2021) 8798–8802.

[24] S. Liu, Y. Fan, Y. Wang, S. Jin, M. Hou, W. Zeng, K. Li, T. Jiang, L. Qin, Z. Yan, Z. Tao, X. Zheng, C. Shen, Z. Liu, T. Ahmad, K. Zhang, W. Chen, Surface-oxygen-rich Bi@C nanoparticles for high-efficiency electroreduction of CO_2 to formate, Nano Lett. 22 (2022) 9107–9114.

[25] D. Yao, C. Tang, A. Vasileff, X. Zhi, Y. Jiao, S.Z. Qiao, The controllable reconstruction of Bi-MOFs for electrochemical CO_2 reduction through electrolyte and potential mediation, Angew. Chem. Int. Ed. 60 (2021) 18178–18184.

[26] Y. Tian, D. Li, J. Wu, J. Liu, C. Li, G. Liu, D. Chen, Y. Feng, Electroreduction of CO_2 to formate with excellent selectivity and stability on nano-dendrite Bi film electrode, J. CO_2 Util. 43 (2021), 101360.

[27] X. Zhou, L. Qian, T. Yu, H. Xiao, L. Liu, Y. Yu, P. Lei, Potential driven volume diffusion in nanoporous AgBi at room temperature, Adv. Funct. Mater. 33 (2023), 2211557.

[28] P. Deng, H. Wang, R. Qi, J. Zhu, S. Chen, F. Yang, L. Zhou, K. Qi, H. Liu, B.Y. Xia, Bismuth oxides with enhanced bismuth-oxygen structure for efficient electrochemical reduction of carbon dioxide to formate, ACS Catal. 10 (2019) 743–750.

[29] H. Yang, N. Han, J. Deng, J. Wu, Y. Wang, Y. Hu, P. Ding, Y. Li, Y. Li, J. Lu, Selective CO_2 reduction on 2D mesoporous Bi nanosheets, Adv. Energy Mater. 8 (2018), 1801536.

[30] L. Zhang, Y. Shi, Z. Wang, C. Hu, B. Shi, X. Cao, Porous β-Bi_2O_3 with multiple vacancy associates on highly exposed active facets for enhanced photocatalytic activity, Appl. Catal. B Environ. 265 (2020), 118563.

[31] W. Huang, Y. Wang, J. Liu, Y. Wang, D. Liu, J. Dong, N. Jia, L. Yang, C. Liu, Z. Liu, B. Liu, Q. Yan, Efficient and selective CO_2 reduction to formate on Pd-doped $Pb_3(CO_3)_2(OH)_2$: dynamic catalyst reconstruction and accelerated CO_2 protonation, Small 18 (2022), e2107885.

[32] A. Zhang, Y. Liang, H. Li, B. Zhang, Z. Liu, Q. Chang, H. Zhang, C.F. Zhu, Z. Geng, W. Zhu, J. Zeng, In-situ surface reconstruction of InN nanosheets for efficient CO_2 electroreduction into formate, Nano Lett. 20 (2020) 8229–8235.

[33] J. Zhu, J. Li, R. Lu, R. Yu, S. Zhao, C. Li, L. Lv, L. Xia, X. Chen, W. Cai, J. Meng, W. Zhang, X. Pan, X. Hong, Y. Dai, Y. Mao, J. Li, L. Zhou, G. He, Q. Pang, Y. Zhao, C. Xia, Z. Wang, L. Dai, L. Mai, Surface passivation for highly active, selective, stable, and scalable CO_2 electroreduction, Nat. Commun. 14 (2023) 4670.

[34] J. Feng, J. Li, L. Qiao, D. Liu, P. Zhou, J. Ni, H. Pan, Reconstructed anti-poisoning surface for enhanced electrochemical CO_2 reduction on Cu-incorporated ZnO, Appl. Catal. B Environ. 330 (2023), 122665.

[35] W. Li, L. Li, Q. Xia, S. Hong, L. Wang, Z. Yao, T. Wu, Y. Soo, H. Zhang, Tsz W. Benedict Lo, A.W. Robertson, Q. Liu, L. Hao, Z. Sun, Lowering C–C coupling barriers for efficient electrochemical CO_2 reduction to C_2H_4 by jointly engineering single Bi atoms and oxygen vacancies on CuO, Appl. Catal. B Environ. 318 (2022), 121823.

[36] P. Deng, F. Yang, Z. Wang, S. Chen, Y. Zhou, S. Zaman, B.Y. Xia, Metal-organic framework-derived carbon nanorods encapsulating bismuth oxides for rapid and selective CO_2 electroreduction to formate, Angew. Chem. Int. Ed. 59 (2020) 10807–10813.

[37] J.M. Dona, J. Gonzalez-Velasco, Mechanism of surface diffusion of gold adatoms in contact with an electrolytic solution, J. Chem. Phys. 97 (1993) 4714–4719.

[38] G. Xi, L. Zuo, X. Li, Y. Jin, R. Li, T. Zhang, In-situ constructed Ru-rich porous framework on NiFe-based ribbon for enhanced oxygen evolution reaction in alkaline solution, J. Mater. Sci. Technol. 70 (2021) 197–204.

[39] S.S. Jeon, P.W. Kang, M. Klingenhof, H. Lee, F. Dionigi, P. Strasser, Active surface area and intrinsic catalytic oxygen evolution reactivity of NiFe LDH at reactive electrode potentials using capacitances, ACS Catal. 13 (2023) 1186–1196.

[40] P. Tan, S. Dimovski, Y. Gogotsi, Raman scattering of non-planar graphite: arched edges, polyhedral crystals, whiskers and cones, Philos. Trans. R. Soc. Lond. A 362 (2004) 2289–2310.

[41] W. Zhang, C. Xu, Y. Hu, S. Yang, L. Ma, L. Wang, P. Zhao, C. Wang, J. Ma, Z. Jin, Electronic and geometric structure engineering of bicontinuous porous Ag–Cu nanoarchitectures for realizing selectivity-tunable electrochemical CO_2 reduction, Nano Energy 73 (2020), 104796.

[42] X. Chen, H. Chen, W. Zhou, Q. Zhang, Z. Yang, Z. Li, F. Yang, D. Wang, J. Ye, L. Liu, Boron dopant induced electron-rich bismuth for electrochemical CO_2 reduction with high solar energy conversion efficiency, Small 17 (2021), e2101128.

[43] W. Shan, R. Liu, H. Zhao, Z. He, Y. Lai, S. Li, G. He, J. Liu, In situ surface-enhanced raman spectroscopic evidence on the origin of selectivity in CO_2 electrocatalytic reduction, ACS Nano 14 (2020) 11363–11372.

[44] J. Fan, X. Zhao, X. Mao, J. Xu, N. Han, H. Yang, B. Pan, Y. Li, L. Wang, Y. Li, Large-area vertically aligned bismuthene nanosheet arrays from galvanic replacement reaction for efficient electrochemical CO_2 conversion, Adv. Mater. 33 (2021), e2100910.

[45] P. Li, J. Bi, J. Liu, Y. Wang, X. Kang, X. Sun, J. Zhang, Z. Liu, Q. Zhu, B. Han, p-d Orbital hybridization induced by P-block metal-doped Cu promotes the formation of C_{2+} products in ampere-level CO_2 electroreduction, J. Am. Chem. Soc. 145 (2023) 4675–4682.

[46] D.J.D. Pimlott, A. Jewlal, B.A.W. Mowbray, C.P. Berlinguette, Impurity-resistant CO_2 reduction using reactive carbon solutions, ACS Energy Lett. 8 (2023) 1779–1784.

[47] Y. Hu, D. Lu, W. Zhou, X. Wang, Y. Li, In situ construction of 3D low-coordinated bismuth nanosheets@Cu nanowire core–shell nanoarchitectures for superior CO_2 electroreduction activity, J. Mater. Chem. A 11 (2023) 1937–1943.

[48] M. Zhao, Y. Gu, W. Gao, P. Cui, H. Tang, X. Wei, H. Zhu, G. Li, S. Yan, X. Zhang, Z. Zou, Atom vacancies induced electron-eich surface of ultrathin Bi nanosheet for efficient electrochemical CO_2 eeduction, Appl. Catal. B Environ. 266 (2020), 118625.

[49] B. Ren, G. Wen, R. Gao, D. Luo, Z. Zhang, W. Qiu, Q. Ma, X. Wang, Y. Cui, L. Ricardez-Sandoval, A. Yu, Z. Chen, Nano-crumples induced Sn-Bi bimetallic interface pattern with moderate electron bank for highly efficient CO_2 electroreduction, Nat. Commun. 13 (2022) 2486.